Spin-Orbit Coupling of Light in Photonic Crystal Waveguides

Moïse Sotto
Sustainable Electronic Technologies, Electronics and Computer Science, Faculty of Physical Science and Engineering, University of Southampton, 8 University Road, Southampton, SO17 1BJ, United Kingdom

Kapil Debnath
Department of Electronics & Electrical Communication Engineering, Indian Institute of Technology Kharagpur, Kharagpur, West Bengal 721302, India

Isao Tomita
Department of Electrical & Computer Engineering, National Institute of Technology, Gifu College, 2236-2 Kamimakuwa, Motosu-city, Gifu 501-0495, Japan

Shinichi Saito*
Sustainable Electronic Technologies, Electronics and Computer Science, Faculty of Physical Science and Engineering, University of Southampton, 8 University Road, Southampton, SO17 1BJ, United Kingdom

(Received 20 December 2018; published 28 May 2019)

We investigate the effect of breaking the parity of a photonic crystal waveguide designed to have odd and even modes intersecting inside the photonic bandgap. The complete study on the wave field properties of the resulting bonding modes uncovers that the transverse spin and orbital parts of the angular momentum couple in the very slow-light regime by means of their local currents. This leads to a subbandgap opening between bands characterized by distinct organizations of this spin-orbit coupling at the nanoscale.

DOI: 10.1103/PhysRevA.99.053845

I. INTRODUCTION

Photonic crystals (PhCs) are the optical analogs of atomic crystal lattices in which dielectric compounds are periodically arranged to shape the propagation of photons [1,2]. In cases where the periodicity and the dielectric contrast are suitably set, complete energy gaps emerge and transform the PhC into a photonic insulator [3–5]. Albeit the amazing confinement properties shown by such a photonic bandgap in itself have important implications for light circuitry on-chip, like the slow-light regime [6–9] and the Purcell effect [10–12], which have been investigated for three decades now, the strong confinement of light provided by PhCs has even more to offer. Cleverly designed structured photonic networks can trigger angular momentum (AM) degrees of freedom like their electronic counterparts: the spin angular momentum (SAM) and the orbital angular momentum (OAM). The SAM is intrinsic and corresponds to circular polarization with left- or right-handedness, while the OAM in its intrinsic form appears as an optical vortex characterized by its topological charge [13–15]. Two-dimensional (2D) PhC hole slabs are well known to support a transverse electric (TE) photonic bandgap, thus photonic crystal waveguide (PCW) modes guided by this bandgap mechanism have a nonparaxial propagation. In other words, the electric field $\vec{E}$ of the confined mode has both transverse and longitudinal components, E_y and E_x, respectively. In the case where these two components have the same magnitude and phase difference $\delta_{xy} = \pm\pi/2$, the electric field is circularly polarized in a plane containing the propagation direction [16,17]. Accordingly, such circularly polarized points (C points) are labeled as transverse SAM and are sometimes referred to in the literature as *photonic wheels* [18–22], which starkly contrasts with the familiar case of an electric field spinning around the propagation axis. The orbital degree of freedom can *a fortiori* be transverse because it is derived from the phase structure of the light. In order to be considered photonic wheels, the optical vortices holding the OAM must wind around an axis perpendicular to the propagation [15,23]. Due to the spatial confinement of light in nanophotonic devices and its evanescent nature in the vicinity of interfaces, numerous on-chip applications are promising for both transverse OAM and SAM ranging from plasmonics to atomtronics as well as silicon (Si) photonics. Topological action is expected to be enabled by the spin-momentum locking, which associates clockwise and anticlockwise rotations with opposite directions of propagation. It has already been demonstrated that photonic wheels are able to directionally excite surface plasmon polaritons at a metal-dielectric interface [24], waveguide modes at the output of a subwavelength microdisk resonator [25], Zeeman sub-levels of a single ultracold atom [26], and even PCW modes through dipolar transitions of quantum dots [27,28]. In all the examples listed, the chiral behavior is derived from a broken symmetry in the system, which limits directional routing in standard PCWs belonging to the symmorphic space group. Locally, angular

*S.Saito@soton.ac.uk

momenta are extremely sensitive to the symmetries, especially in inhomogeneous media [29,30] like PhCs. Thus the break of important symmetries like rotational [31,32] and inversion [33,34] symmetry opens a nontrivial gap between bands characterized by different Chern numbers [35,36]. Symmorphic PCWs confine pairwise modes with both odd and even symmetries that can intersect without interacting with each other due to their different parities [9,37]. Breaking the parity by substituting the mirror symmetry with a glide-plane symmetry allows a branch exchange between these modes raising the degeneracy [38–40], which is somehow reminiscent of the spin-orbit coupling effect on energy bands in atomic crystals [41]. Inducing spin and orbital fluxes in photonic systems is a crucial step towards the realization of directional routing for light circuitry on-chip and hence architect scalable photonic networks with logic gates able to deliver different outputs distinct in their directionality. It is the purpose of this work to understand the nature of spin and orbital currents in the anomalous slow-light regime of a photonic bandgap and highlight the interplay between OAM and SAM at the nanoscale as well as study how these wave field properties can be engineered through modification of the planar structure in order to possibly functionalize them for the next generation of optical communication protocols.

Here, we present a comprehensive study of the anticrossing taking place when the parity of a symmorphic PCW is broken and its impact on both the spin and the orbital AM local currents in the particular context of zero group velocity (ZGV) [15,42,43]. A clear picture of the wave fields is obtained by using the three-dimensional finite-difference time-domain (3D-FDTD) method and leads to the main result: a gap opens between bands that encapsulate different organizations of the spin-orbit coupling at the nanoscale. In Sec. II, we emphasize the consequence of breaking the parity on the photonic band structure and point out how it gives rise to the formation of hybrid modes neither odd nor even accompanied by the emergence of the slow-light regime at an anomalous position in the Brillouin zone. Section III presents the properties of the cycle-averaged electromagnetic fields in the plane of symmetry ($z = 0$) of the PCW. The transverse SAM and OAM are clearly identified by means of the Stokes parameters and analysis of the modal phase structure, respectively. The analysis of the electromagnetic fields reveals that photonic wheels do not necessarily vanish as the light slows down in a PCW. Furthermore, the influence of the optical vortices on the state of polarization is highlighted by examining its evolution on the Poincaré sphere and reveals that the OAM acts as an effective polarization for the envelope streamlines. Finally, in Sec. IV we move from the previously used 2D description of the modal properties to a 3D analysis of the SAM and OAM densities with the appropriate Minkowski formalism [29,30,44]. These quantities, representing the local fluxes of the respective angular momenta, provide deeper insight into the structure of the light and allow one to understand how the nonparaxial guidance and the slowdown effect, induced by the photonic bandgap, organize the SAM (OAM) by means of the OAM (SAM) density. These features represent a clear manifestation of the spin-orbit coupling in this PCW occurring at subwavelength dimensions. Outlooks on the potential applications of controlling the SAM and OAM of light at the nanoscale are given in Sec. IV to conclude the paper.

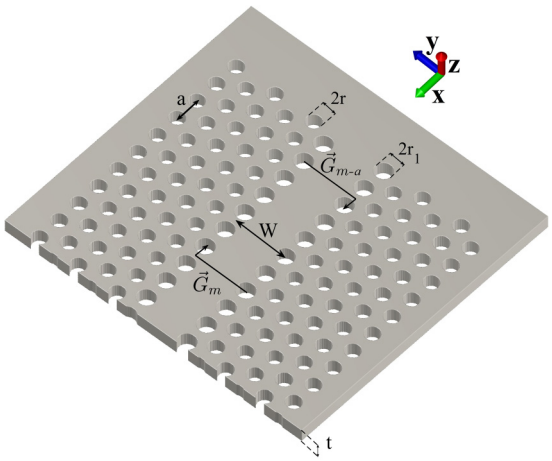

FIG. 1. The PhC is a hexagonal lattice of period $a = 0.415$ nm patterned with holes of radii $r = 0.3a$ in a Si slab of thickness $t =$ 220 nm. The waveguide has a width $W = 1.3\sqrt{3}a$ and the first rows of holes have a modified radius of $r_1 = 0.35a$. One side of the PhC is shifted along the propagation direction by an offset m with respect to the other, as the mirror symmetry is replaced by the glide-plane axis $\vec{G}_m$ and $\vec{G}_{m-a}$.

II. BAND STRUCTURE: EFFECT OF BREAKING THE PARITY SYMMETRY

Recently, the tight confinement offered by 2D PhCs and the resulting nonparaxial guidance of light enabled manipulation of the directional emission of an embedded quantum emitter by engineering the density of photonic states at C points [27]. This effect is salient in nonsymmorphic PCWs [39], where the mirror symmetry of the structure is replaced by glide-plane symmetries. To qualitatively explain why, we propose to express the field intensity at the center of a symmorphic PCW, in terms of left circularly polarized (LCP) and right circularly polarized (RCP) vectors $[\vec{E}_{\circlearrowleft}/\vec{E}_{\circlearrowright} = (E_x\vec{x} \pm iE_y\vec{y})/\sqrt{2}]$. The longitudinal and transverse electric components of a TE-guided mode have opposite parities given by the relations

$$\begin{aligned} E_x(x, y, z) &= \pm E_x(x, -y, z), \\ E_y(x, y, z) &= \mp E_y(x, -y, z), \end{aligned} \tag{1}$$

where the mode parity is classified with respect to the transverse component. It follows that the RCP and LCP components have the same norm and a phase difference $\delta_{\circlearrowleft\circlearrowright} = 0$ or $\pm\pi$ at $y = 0$. Therefore, the degree of ellipticity is null where the electric field is maximum.

On the contrary, breaking the PCW parity makes the parity classification of Eq. (1) obsolete [39], thus allowing chiral and high-field-intensity regions to overlap. The design parameters used to form such hybrid bands are represented in Fig. 1. The $1.3\sqrt{3}a$ wide PCWs (y component of the center-to-center distance between two holes bordering the waveguide) are formed in a hexagonal lattice of period $a = 415$ nm patterned with holes of radii $r = 0.3a$ in a 220-nm-thick Si slab, and the radii of the first rows of holes are extended to $r_1 = 0.35a$.

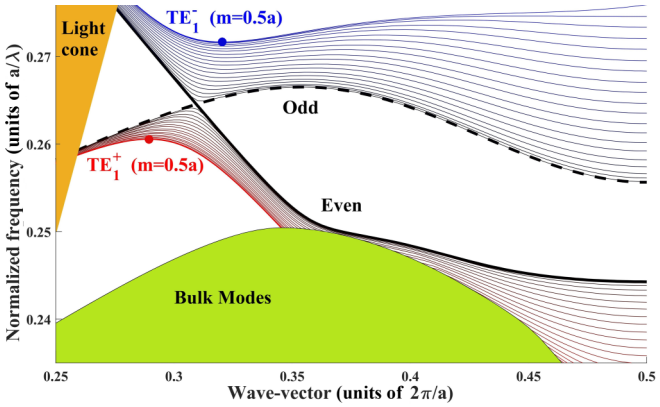

FIG. 2. Band structures of the PCW for different offset m's between the two sides of the PhC. PhC bulk modes are represented in green, and the light cone in orange. The dispersion relation for the symmorphic structure ($m = 0$) is represented by dashed and solid black lines for the odd and even modes, respectively. The offset couples the odd and even modes, which gives rise to the TE_1^+ and TE_1^- modes, in shades of red and blue, respectively. These modes are represented in red and blue for the maximum offset $m = 0.5a$ and their anomalous ZGV points are represented by red and blue circles, respectively.

One side of the PhC is shifted, with respect to the other, by an offset m along the propagation direction. In this instance, the mirror symmetry operations, Eq. (1), are replaced by the glide-plane transformations as

$$\hat{G}_m\vec{E}(x, y, z) = e^{imk}\vec{E}(x, -y, z),$$
$$\hat{G}_{m-a}\vec{E}(x, -y, z) = e^{i(m-a)k}\vec{E}(x, y, z), \quad (2)$$

where $\hat{G}_m$ is the glide-plane operator and $y > 0$.

The transformation of the band structure, calculated by the 3D-FDTD method, as m is scanned from 0 to $a/2$ is shown in Fig. 2. Modes originally crossing, due to their different parities under mirror symmetry, bond together and exchange their branches in such a way that ZGV points appear far from the edge of the Brillouin zone. At such wave vectors ($ka \neq \pm\pi, 0$), which represent anomalous positions for the slow-light regime of a PCW [42,43], geometrical phases are not inhibited and the energy flux represented by the Poynting vector,

$$\vec{\mathcal{P}} = \tfrac{1}{2}\mathrm{Re}(\vec{E} \times \vec{H}^*), \quad (3)$$

cannot simply vanish everywhere as is the case at the band edge [15]. On the other hand, the total energy flow passing through the PCW unit cell must be null in order to also satisfy its scalability with the group velocity.

III. ELECTROMAGNETIC WAVE PROPERTIES

Here, the properties of the electromagnetic fields are presented. Henceforth, the even and odd (TE_1^+ and TE_1^-) modes are referred to as the crossing points (their respective anomalous ZGV points) without any ambiguity. The electric and magnetic field profiles are distinctively described in the plane of symmetry to emphasize that they hold separate parts of the AM. Nevertheless, the first indication of the interplay between the spin and the orbital AM in both bonding modes is presented through the energy streamlines.

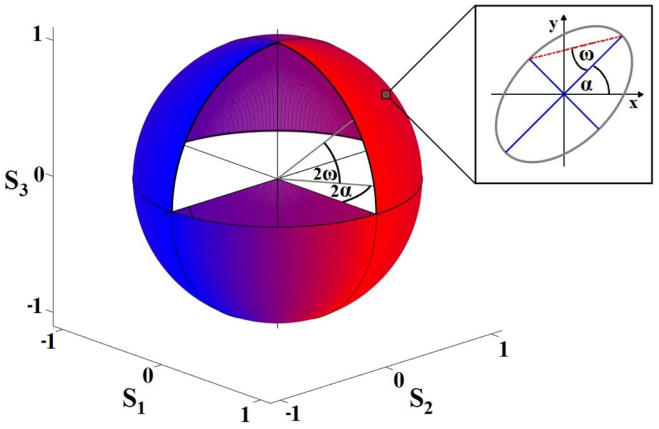

FIG. 3. The Poincaré sphere can be represented by the Stokes parameters S_1, S_2, and S_3 in the Cartesian coordinate system or in the spherical coordinate system with angles α and ω, parametrizing the polarization ellipse (inset), times a factor of 2.

A. Electric field properties: Stokes parameters, Poincaré sphere, and SAM

In a PCW slab, the light is completely polarized in the plane of symmetry ($z = 0$) [45], as the guided modes there have orthogonal electric and magnetic fields. For instance, the field components of a TE mode are expressed by

$$\vec{E}(x, y, z = 0) = (E_x, E_y, 0),$$
$$\vec{H}(x, y, z = 0) = (0, 0, H_z). \quad (4)$$

Therefore, the polarization can be characterized in this plane by using the Stokes parameters,

$$S_0 = |E_x|^2 + |E_y|^2,$$
$$S_1 = |E_x|^2 - |E_y|^2 = S_0\cos(2\omega)\cos(2\alpha),$$
$$S_2 = 2\mathrm{Re}(E_x^* E_y) = S_0\cos(2\omega)\sin(2\alpha),$$
$$S_3 = 2\mathrm{Im}(E_x^* E_y) = S_0\sin(2\omega), \quad (5)$$

which respect the full polarization condition [46],

$$\sum_{i=1,2,3} S_i^2(x, y, 0) = S_0^2(x, y, 0). \quad (6)$$

The Stokes parameters S_1, S_2, and S_3 refer to the description of the polarization in the linear (E_x, E_y), diagonal ($E_x + E_y$, $E_x - E_y$)/$\sqrt{2}$, and circular ($E_\circlearrowleft$, $E_\circlearrowright$) polarization bases, respectively. Their complementarity allows the state of polarization to be represented as a point on the surface of the Poincaré sphere [13,14,46] as shown in Fig. 3, which is also defined by the azimuthal and polar angles 2α and 2ω introduced in the third set of Eq. (5). These angles also characterize the polarization ellipse times a factor of 1/2 (see Fig. 3 inset). This factor comes from the fact that the rotation of the polarization state on the surface of the Poincaré sphere has an SO(3) representation, while the polarization ellipse can be transformed through the Jones calculus equivalent to SU(2) transformations and typical of a spin-half system.

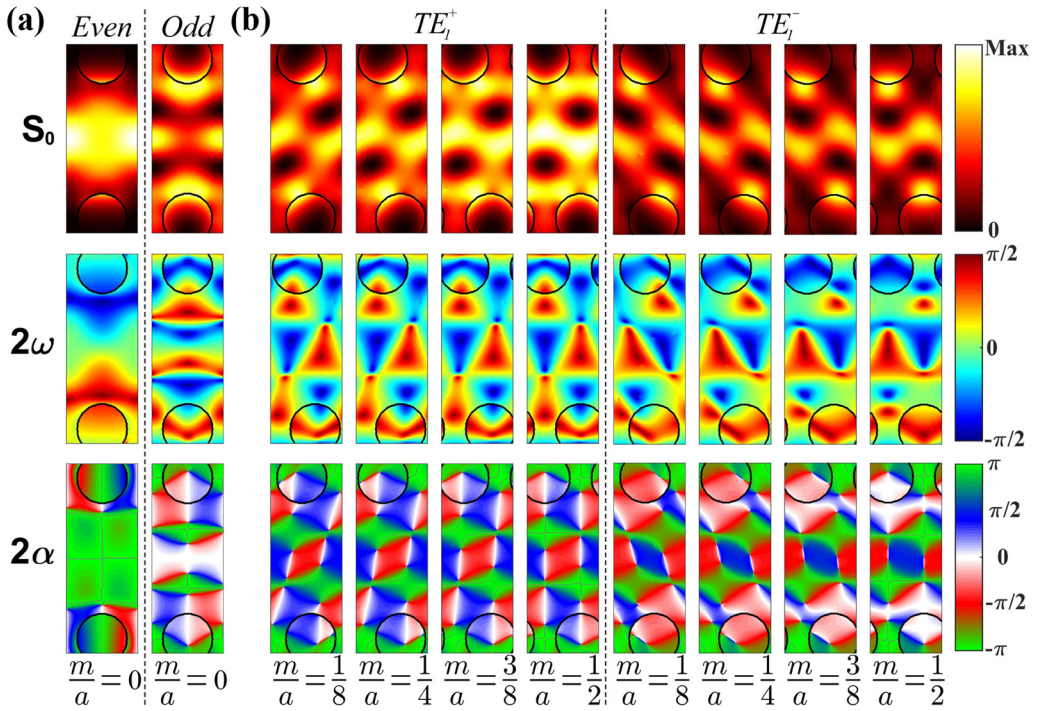

FIG. 4. Polarization characteristics (a) of the pairwise modes in the symmorphic structure and (b) of the TE_1^+ and TE_1^- modes for different m's. Top panels represent the Stokes parameter S_0, which is normalized with respect to the highest field intensity in each graph. Middle and bottom panels describe the angles 2ω and 2α within the PCW unit cell, respectively.

Figure 4 displays the spatial profiles of S_0, 2α, and 2ω in the PCW unit cell for odd and even modes at the crossing points as well as for TE_1^+ and TE_1^- modes with different m's. The RCP (LCP) locations are depicted by $2\omega = \pm\pi/2$ but have an undefined 2α. It can be noted in the relevant figures that at these particular points, all the 2α values are merging towards the C points. Since the electric fields of the even and odd modes are mostly linearly polarized along the transverse and longitudinal direction, respectively, C points do not coincide with high-intensity regions in the symmorphic configuration, as shown in Fig. 4(a). The difference in their polarization arises from their distinct guidance mechanisms. The even mode is index guided and experiences the PhC as a periodic corrugation; its confinement relies only on the total internal reflection. On the other hand, the odd mode is guided by the photonic bandgap and penetrates into the PhC bulks. The Bragg mechanism enforces this mode to have its dominant electric field component parallel to the direction of propagation.

Nevertheless, the situation is rather different once the parity symmetry is broken, as shown in Fig. 4(b). The branch exchange between these modes with orthogonal dominant polarizations results in bonding modes not only supporting C points in high-field-intensity regions but also providing a degree of ellipticity to the electric field maxima. Here, the interest comes from the fact that the SAM arises despite the ZGV, while in standard PCWs, if the band edge is generally the region of the slow-light effect, the matching of the wave vector with the periodicity annihilates the chirality because the associated fields become purely real:

$$\lim_{k\to\frac{\pi}{a}} \mathrm{Im}(\vec{\mathrm{E}}) \to \vec{0}. \tag{7}$$

Conversely, modes guided by wave vectors different from high-symmetry points of the Brillouin zone must be associated with fields having a nonzero imaginary part because the translation of a period induces a phase shift of $\neq 0$ or $\pm\pi$. In our case, it can be concluded that breaking the parity symmetry is beneficial to form hybrid modes holding enhanced transverse SAM at anomalous ZGV points, showing that photonic wheels do not always stop turning when the light slows down in a PCW.

B. Magnetic field properties: Vortices, topological charge, and OAM

In the former part, it has been shown that the electric fields of the bonding modes carry the transverse SAM degree of freedom, which is conserved by the periodicity (translation by a period) and reversed by the glide-plane axes $\vec{\mathrm{G}}_m$ and $\vec{\mathrm{G}}_{m-a}$. Therefore, it is natural to examine the properties of the magnetic field in the plane of symmetry and seek the presence of another AM: the orbital degree of freedom.

The intensity as well as the phase,

$$\theta = \arg(\mathrm{H}_z), \tag{8}$$

profiles are reported in Figs. 5(a) and 5(b) for the even and odd modes in the top and middle panels, respectively. In order to study the impact of the guidance mechanism on the field properties, $\vec{\mathcal{P}}$ is superimposed onto the phase pattern of the modes. As seen previously, the even mode does not differ fundamentally from a single mode in a normal ridge Si waveguide, except by its backward propagation due to the periodicity. All the energy flows are confined within the core of the waveguide, a region that was previously characterized

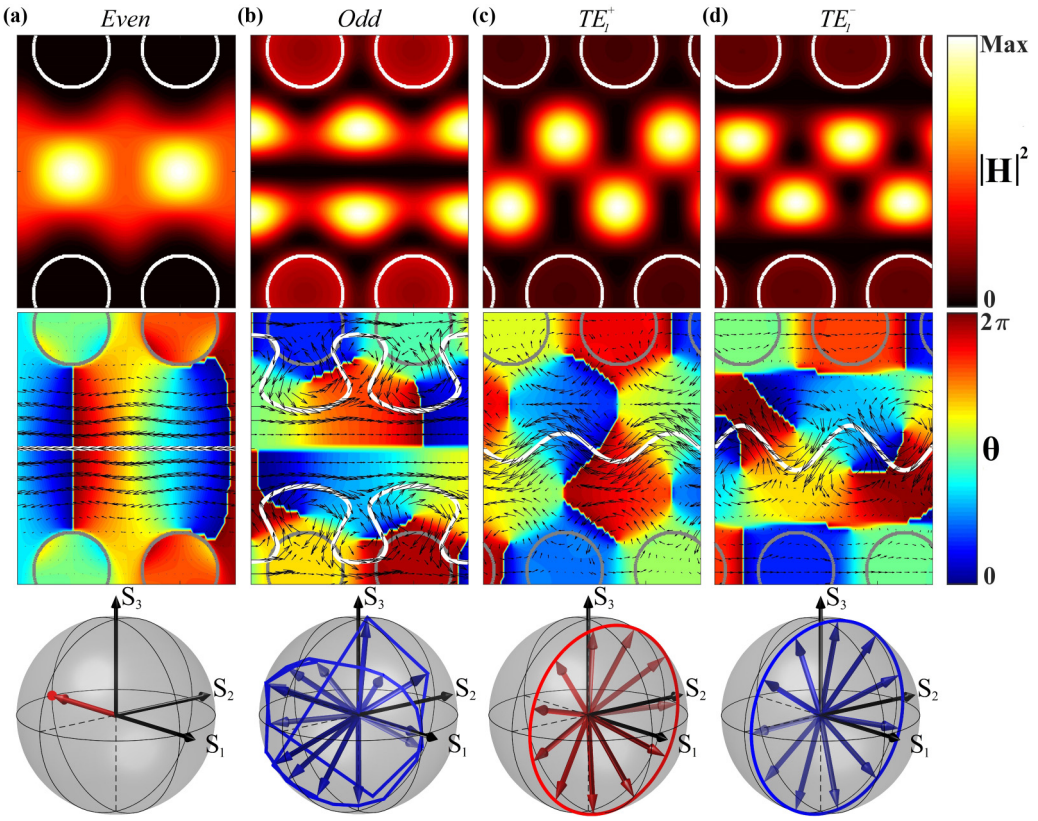

FIG. 5. Magnetic field properties of the (a) even, (b) odd, (c) TE_1^+, and (d) TE_1^- modes in the plane of symmetry of the PCWs. Top panels represent the magnetic field intensity of the modes $|H|^2$. In the middle panels, the phase patterns θ of the modes are represented by contour plots on which black arrows, corresponding to the Poynting vector $\vec{\mathcal{P}}$, have been superimposed. White lines are the major energy streamlines. The polarization along these streamlines has been plotted on the Poincaré sphere in the bottom panels. The opacity of the polarization vector increases along the propagation. For simplicity, only the streamline in the upper part of the PCW ($y > 0$) is represented for the odd mode (b).

as being polarized along $\vec{y}$ [Fig. 4(a)]. The polarization along the major streamline of $\vec{\mathcal{P}}$ is reported in the bottom panel in Fig. 5(a) and clearly shows that the light flows without changing its polarization. On the contrary, the odd mode, shown in Fig. 5(b), is guided by the photonic bandgap and presents a group index an order of magnitude higher than the even-mode group index due to the presence of a folded K point in the band structure [37]. The intensity pattern shows that the magnetic field not only is confined in the central region but also extends into the PhC bulks. Due to the higher order of this mode, one can distinguish a few lobes with nodes between them. Its phase pattern has a strong modulation with a patchy structure and emphasizes that the aforementioned nodes are the centers of optical vortices. The phase is undetermined at the center of the vortices and jumps by $\pm 2\pi$ around them such that

$$l = \frac{1}{2\pi} \int_L \vec{\nabla}(\theta) \cdot d\vec{s} = \pm 1 \tag{9}$$

is the topological charge of these vortices, where L is a closed clockwise contour around a vortex. The energy flow is circulating around the phase singularities and propagates by undulating between vortices with opposite topological charges, which reflects the slowdown factor of this mode in the real space. However, the polarization along the propagation of the major energy streamline describes a complex evolution, as shown in the bottom panel in Fig. 5(b). The $\frac{a}{80} \times \frac{a\sqrt{3}}{160} \times \frac{t}{10}$ mesh used for the simulation is not accurate enough to represent the evolution of the state of polarization as continuous on the Poincaré sphere. It should be further noted that the streamlines are guided by optical vortices without symmetry operations linking them. Altogether, it reflects that abrupt changes of both 2α and 2ω occur along the path. This is supported by comparison with Fig. 4(b), which displays a strong modulation of both parameters in the vicinity of the streamline.

The situation is rather different for the bonding modes. For simplicity, only the maximum offset $m/a = 1/2$ is explored henceforth. It can be noted in the middle panels of Figs. 5(c) and 5(d) that the optical vortices organize the local currents of energy so that the total flow is null with respect to the ZGV. The energy fluxes in the PhC bulks and inside the waveguide propagate in opposite directions and spiral energy currents appear between them. If the major streamlines are also circulating between optical vortices with opposite topological charges for both modes, the optical vortices are not located near the PhC parts but rather inside the waveguide. It is immediately apparent that the phase structure of the TE_1^+ mode has a strong phase modulation extending all over the structure, with phase gradients forcing one vortex to

bond with three vortices characterized by opposite topological charges. The phase pattern of this mode takes the form of shrunken hexagons reminiscent of the structural arrangement of graphene. On the other hand, the phase modulation of the TE_1^- mode is constrained within the core of the waveguide so that the vortices only bond through the glide-plane symmetry and thereby form a chain similar to polyacetylene. These similarities to organic chemistry come from the triangular lattice, suggesting that other arrangements of singularities may be formed by choosing another crystal lattice.

The optical vortices present in the field pattern of these modes play a completely different role with regards to the evolution of the polarization along the major streamline. It is well known that vortex beams in free space like Laguerre-Gaussian beams of higher order possess a longitudinal OAM around which the polarization rotates in the S_1S_2 plane [13,14]. This means that the parameter 2α is periodically evolving over $2\pi c/\lambda$ in these beams. In our case, if the net orbital momentum of the PCW modes is null, the transverse aspect of the optical vortices seems to contribute in a different way to the motion of the polarization state on the Poincaré sphere. For both the TE_1^+ and the TE_1^- modes, their polarization vectors rotate in the S_2S_3 plane around a constant S_1 value, as shown in the bottom panels in Figs. 5(c) and 5(d). The difference in their S_1 values can be associated with the spanning of the vortices in the y direction. In the case of the TE_1^+ mode, their proximity limits the swinging amplitude of the energy flow. Simultaneously, the degree of ellipticity decreases shortly outside the C points, while for the TE_1^- mode, the ellipticity remains important in the transverse direction outside the SAM locations, as the major energy streamline smoothly turns around the vortices. Nevertheless, their polarization vectors turn in the anticlockwise direction in both cases, but with a π-shift difference: the polarization of the TE_1^+ (TE_1^-) mode is described by $2\alpha = \pi/2$ ($2\alpha = -\pi/2$) at the border of the unit cell [cf. bottom panel in Fig. 4(b)]. Depending on the nature of the system and the variable relevant to its dynamic, the evolution of the state of polarization may be described by a type equation similar to a famous classical, relativistic, or quantum law like the Lorentz pseudoforce [47], the Schrödinger equation [48], and the Larmor precession equation [49]. In the case of such a nonsymmorphic PCW ($m \neq 0$), the glide-plane symmetry guarantees that the global chirality is null:

$$\int_{-\infty}^{\infty}\int_{0}^{a} S_3(x,y)dxdy = 0,$$
$$S_3(x,y) = -S_3(x+m,-y) = -S_3(x+m-a,-y). \quad (10)$$

By referring to the correspondence between the spin of light and the electronic spin, the complete rotation of the polarization along the energy flux is analogous to spin waves in antiferromagnetic materials [50] and thus can be described by a modified Landau-Lifshitz equation of motion without damping [51]:

$$\frac{d}{dt}\begin{pmatrix}S_1\\S_2\\S_3\end{pmatrix}\frac{1}{S_0} = -\frac{2\pi c}{\lambda}\begin{pmatrix}S_1\\S_2\\S_3\end{pmatrix}\frac{1}{S_0}\times\vec{P}_{\text{eff}}, \quad (11)$$

where $\vec{P}_{\text{eff}}$ is an effective polarization driving the precession of the polarization state. As the analysis is conducted on streamlines guided by the optical vortices, the polarization state at the center of the vortices would be the natural choice for this parameter. Indeed, Eq. (10) links the polarization of two opposed topological charges related by the glide-plane symmetry and therefore makes the S_1 component the relevant Stokes parameter to consider. Surprisingly, the projected electric field is oriented there along the y axis for both the TE_1^+ and TE_1^- modes ($2\alpha = \pi$) and thus makes Eq. (11) absolutely valid by setting $\vec{P}_{\text{eff}} = (-1,0,0)$. This dynamic reveals that the alternative transverse OAM progressively inverts the SAM through the glide-plane symmetry and makes the evolution of the periodic chirality pattern similar to the fundamental state of an ordered Haldane spin chain with Bloch walls [50,52]. The other energy streamlines trapped between the optical vortices also form circular contours on the Poincaré sphere surface but their effective polarizations have a nonzero 2ω value. Being an affair of polarization, a qualitative description of these streamlines by Eq. (11) remains true as the ellipticity of the effective polarization vector is in line with the proximity of one or another vortex. However, an appropriate charge potential-like, decaying with the relative distance of the streamlines with $l = 1$ and $l = -1$ topological charges, must be taken into account to quantitatively picture the evolution of the polarization along these streamlines.

IV. AM DENSITIES AND SPIN-ORBIT COUPLING

If the properties of the electromagnetic fields have been synthesized in the plane of symmetry, it is because the PCW modes are confined in a dielectric slab as thick as $\frac{\lambda}{2n_{\vec{S}_i}}$ and hence are fundamental in the z direction. This allows $\vec{E}$ and $\vec{H}$ to be reduced to 2D scalar distributions of their phase and intensity. However, this simplification cannot be made for other wave fields that characterize the PCW modes and require a 3D analysis to completely depict their properties. This is especially true for the SAM and the OAM densities, which retain their significance even where the light is partially polarized [1,45,46]. Recent interest in optical momenta, including photonic wheels, leads towards a deeper understanding of the dynamics of such wave fields in inhomogeneous media. The main interest in studying these characteristics lies in their canonical aspects; they enable the description of the structured field beyond its kinetic picture. For example, the study of these quantities has yielded theoretical results that demonstrate the conservation and the quantization of the total AM number for modes confined in cylindrical fibers and metallic wires [30], as well as the transverse character of the spin of a surface plasmon polariton at a metal-vacuum interface [53,54], which has been proven to be equal to the electron spin contribution per plasmon at its maximum frequency [29].

Nevertheless, to the best of our knowledge, the local currents of spin and orbital angular momenta have not been explored in PhCs yet. Only the SAM density has been described in the plane of symmetry to explore the nonzero chirality of a PCW mode trapped between different PhCs with trivial and nontrivial photonic bandgaps [55], thus ignoring its vectorial nature. Defining both the SAM and the OAM densities across

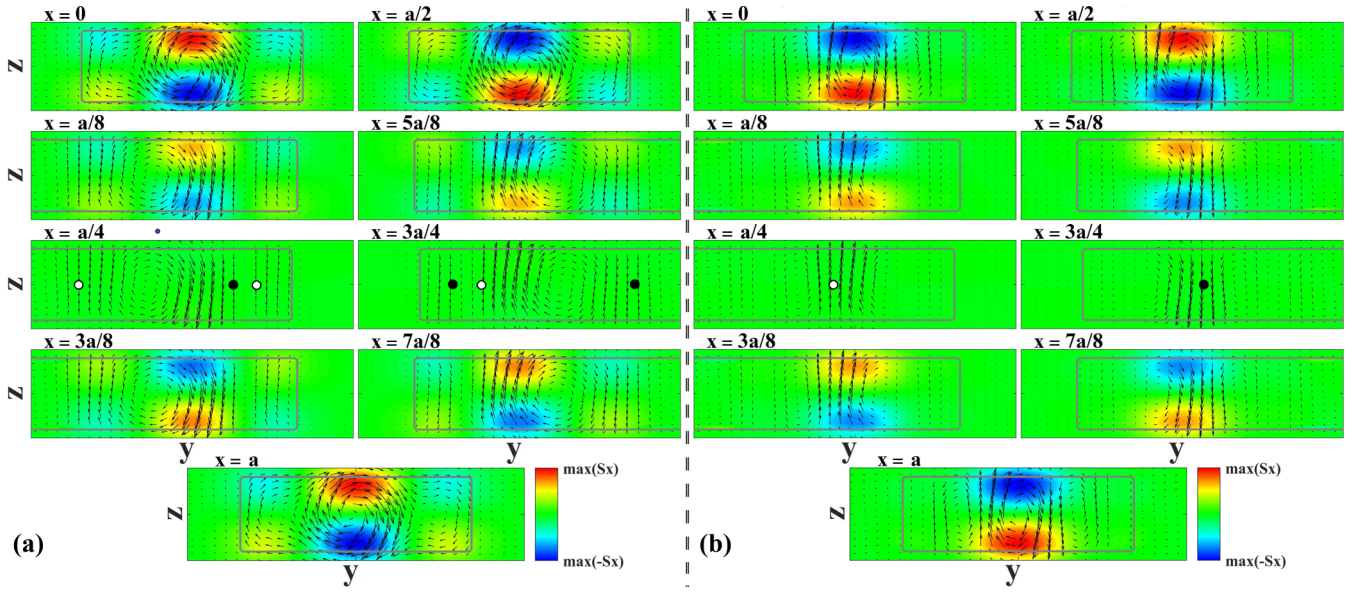

FIG. 6. SAM density of the (a) TE_1^+ and (b) TE_1^- modes along the propagation direction at different x positions in the unit cell. Arrows describe the components S_y and S_z transverse to the propagation, while the colored plot represents the longitudinal component S_x. The vortex centers with topological charges $l = \pm 1$ are represented by white and black circles, respectively.

the PhC slab reveals interesting properties of the optical AM brought by both the photonic bandgap and the total internal reflection. According to the developed formalism based on the Minkowski description of the light [29,30,44], the linear (canonical) momentum, the SAM, and the OAM densities can be expressed in our system as

$$\begin{aligned}\vec{\mathrm{P}} &= \frac{\lambda}{8\pi c}\mathrm{Im}(\epsilon\vec{\mathrm{E}}^*.\vec{\nabla}(\vec{\mathrm{E}}) + \mu\vec{\mathrm{H}}^*.\vec{\nabla}(\vec{\mathrm{H}})),\\ \vec{S} &= \frac{\lambda}{8\pi c}\mathrm{Im}(\epsilon\vec{\mathrm{E}}^* \times \vec{\mathrm{E}} + \mu\vec{\mathrm{H}}^* \times \vec{\mathrm{H}}),\\ \vec{L} &= \vec{r} \times \mathrm{P}, \end{aligned} \tag{12}$$

respectively, where ϵ is the permittivity and μ is the permeability of the dielectrics. As the dimensions of the PCW set the frequencies of the modes in the telecom bandwidth, any dispersion corrections from both air and Si are neglected. As mentioned before, any geometrical phases must vanish at the band edge and the same applies to the AM densities. Therefore, the anomalous ZGV points represent the appropriate framework to analyze the coaction between slow light and AM and can provide deeper insight into the nature of photonic wheels in the slow-light regime.

A. SAM density

Since the SAM density is, by definition, normal to the polarization ellipse, it is limited to the electric field contribution only in the plane of symmetry. Furthermore, restricting the analysis of the SAM density to this plane conceals the local currents in the x and y directions. For instance, if it has been shown in the previous section that the PCW modes are locally chiral, their helicity density [$\propto \mathrm{Im}(\vec{\mathrm{E}} \cdot \vec{\mathrm{H}}^*)$] is identically 0 in the plane of symmetry [see Eq. (4)] and remains weak inside the slab due to the TE-like polarization [1]. As the helicity measures the alignment of the spinning axis with the linear momentum, the polarization conditions substantiate not only that the SAM at $z = 0$ has a pure transverse character, but also that the SAM density propagation is exclusively normal to the xy plane there. Still, the PCW has a one-dimensional periodicity and the modes are guided by global wave vectors parallel to the x axis; it is therefore natural to examine the behavior of the SAM density along the propagation.

Figures 6(a) and 6(b) depict the SAM density in the yz plane at different x positions in the unit cell, for both the TE_1^+ and the TE_1^- modes, respectively. The arrows represent the projection of the SAM density in the yz plane, while the colored contour plot represents the longitudinal component. The striking feature of the transverse components is the emergence of circular and spiral flows of the transverse component of the SAM inside the PCW slab. Moreover, it can be noted that the SAM density is exclusively oriented along the z axis in the plane of symmetry because only the electric field contributes to the SAM there. If it is mandatory to analyze the 3D structure of the AM densities in order to fully characterize these wave fields, the fact remains that the glide-plane axis is a pure 2D concept. Therefore, the relevant symmetry to characterize the AM density needs to be reconsidered. As the system also has a mirror symmetry in the z direction, the combination of both symmetries is nothing but a twofold screw axis. Figure 6 illustrates that the sense of circulation of the SAM density in the xy plane seems to be conserved by the screw rotation. Indeed, the longitudinal component is even while the transverse component is odd with respect to this symmetry:

$$\begin{pmatrix} S_x \\ S_y \\ S_z \end{pmatrix}(x, y, z) = \begin{pmatrix} S_x \\ -S_y \\ -S_z \end{pmatrix}(x + a/2, -y, -z). \tag{13}$$

In addition to that, the longitudinal component of the SAM density is odd with respect to the mirror symmetry along the

z direction,

$$S_x(x, y, z) = -S_x(x, y, -z), \tag{14}$$

which ensures that the total SAM does not possess a net total momentum along the direction of propagation. This organization of the SAM density flows translates to a closed circulation trapping nonvanishing fluxes inside the dielectric that inverse the sign of the transverse spin in the plane of symmetry. This inversion is inherent to the conservation of the permittivity by glide-plane symmetry as well as its isotropy. Although this is beyond the scope of this work, an inhomogenous PCW system made of anisotropic materials, filled with liquid crystal [56,57], for example, may perhaps be able to present a pure transverse spin with unique handedness [58]. Nevertheless, the nonsymmorphic PCW studied here possesses other symmetry operations [39], namely, the convolution of the translation by $a/2$ and the mirror reflection σ_x at $x = a/4$ and $3a/4$. Interestingly, the longitudinal component of the SAM density is null at these positions that coincide with the topological charges. In order to examine the structure of the local currents from another perspective, the SAM density is represented by arrows in the xy plane at different heights ($z = \pm t/4$) for both the TE_1^+ and the TE_1^- modes in Figs. 7(a) and 7(b), respectively, and superimposed on the θ pattern of the modes at $z = 0$. The calculation shows that the topological charges l generate SAM density fluxes which lead towards vortices with opposite topological charges. One aspect of the spin-orbit coupling of the PCW modes studied is revealed here: the organization of the relevant spin current shows that the optical vortices, holding the OAM, play the role of waypoints for the SAM density in such a way that, through the SAM density fluxes, an optical vortex bonds with its neighboring vortices that have an opposite topological charge. This arrangement of the SAM wave field, with respect to the topological charges, is similar to the magnetic field streamlines established between two magnetic dipoles in an antiparallel configuration and qualitatively explains why the sign of the topological charge determines the direction of the SAM density, along the z axis. Furthermore, Fig. 7 also discloses that the streamlines of $\vec{S}$ follow constant θ values such that the circulation of the SAM density cannot be established between optical vortices with the same topological charge. Pieced together, these characteristics draw a clear picture of the SAM density circulation that can be summarized as follows: the bonding modes can be compared at different arrangements of spins oriented in the opposite direction of their first neighbors, confirming the antiferromagnet analogy developed in the former section. It is also in agreement with the Ising picture of antiferromagnetic materials [59] (i.e., a negative exchange constant between the first-neighbor spins). For the TE_1^+ mode, topological charges bond with three opposite topological charges, while with only two for the TE_1^- mode, thus qualitatively explaining why they are the lower and upper energy levels, respectively.

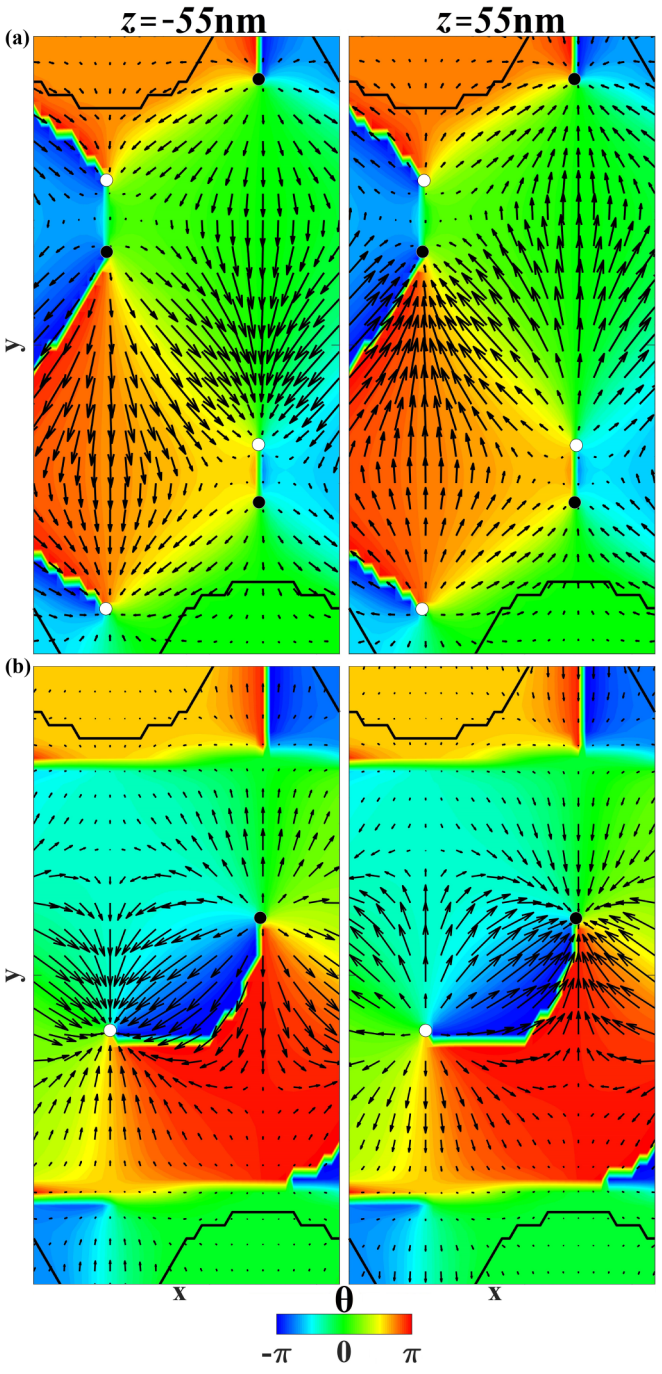

FIG. 7. SAM density projected on the xy plane at $z = \pm t/4$ for the (a) TE_1^+ and (b) TE_1^- modes. The projection is represented by black arrows; the phase pattern of the magnetic fields θ, by the colored plot; and topological charges $l = \pm 1$, by white and black circles, respectively.

B. Linear momentum and OAM densities

The linear momentum density is an interesting property quantifying the propagation direction of the electric and magnetic fields. It can be interpreted as a local wave vector of the modes. As the modes are considered in the special framework of the ZGV, the overall linear momentum flow along the propagation direction must cancel because the fields carry the electromagnetic energy. Nevertheless, the inhomogeneity at the subwavelength scale of any PhC system goes hand in hand with the fact that the electromagnetic field is not dual symmetric, as is the case for waves propagating in an isotropic and homogeneous medium. This lack of dual symmetry comes along with the fact that the spin is not aligned with the

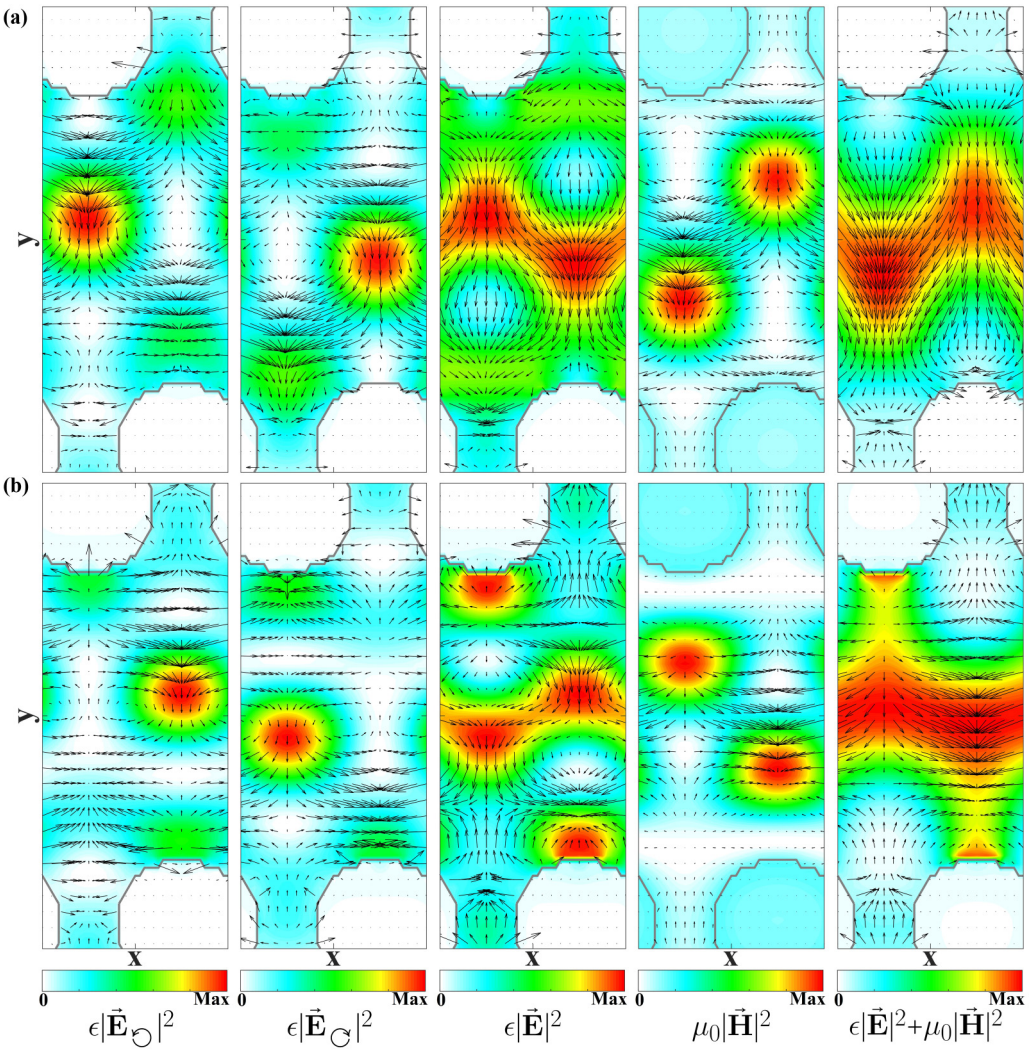

FIG. 8. Linear AM density components of the (a) TE_1^+ and (b) TE_1^- modes represented by black arrows and superimposed on the energy density profiles from left to right: LCP contributions, RCP contributions of the electric field, total electric fields, magnetic fields, and total electromagnetic fields.

helicity. If this constitutes a strong basis for seeking evidence of the spin-orbit coupling in these systems [60], it also implies that both $\vec{\mathrm{E}}$ and $\vec{\mathrm{H}}$ contributions have to be accounted for in order to properly define any momentum densities. The linear momentum density can be split into electric and magnetic parts. Similarly, the electric field part of the linear momentum density can be decomposed into an LCP, an RCP, and an out-of-plane contribution for each component, which allows for a separate representation

$$\epsilon\vec{\mathrm{E}}^*\cdot\vec{\nabla}(\vec{\mathrm{E}}) = \epsilon\begin{pmatrix} \mathrm{E}_x^*\frac{\partial \mathrm{E}_x}{\partial x}+\mathrm{E}_y^*\frac{\partial \mathrm{E}_y}{\partial x}+\mathrm{E}_z^*\frac{\partial \mathrm{E}_z}{\partial x} \\ \mathrm{E}_x^*\frac{\partial \mathrm{E}_x}{\partial y}+\mathrm{E}_y^*\frac{\partial \mathrm{E}_y}{\partial y}+\mathrm{E}_z^*\frac{\partial \mathrm{E}_z}{\partial y} \\ \mathrm{E}_x^*\frac{\partial \mathrm{E}_x}{\partial z}+\mathrm{E}_y^*\frac{\partial \mathrm{E}_y}{\partial z}+\mathrm{E}_z^*\frac{\partial \mathrm{E}_z}{\partial z} \end{pmatrix} = \epsilon\begin{pmatrix} \mathrm{E}_{\circlearrowleft}^*\frac{\partial \mathrm{E}_{\circlearrowleft}}{\partial x}+\mathrm{E}_{\circlearrowright}^*\frac{\partial \mathrm{E}_{\circlearrowright}}{\partial x}+\mathrm{E}_z^*\frac{\partial \mathrm{E}_z}{\partial x} \\ \mathrm{E}_{\circlearrowleft}^*\frac{\partial \mathrm{E}_{\circlearrowleft}}{\partial y}+\mathrm{E}_{\circlearrowright}^*\frac{\partial \mathrm{E}_{\circlearrowright}}{\partial y}+\mathrm{E}_z^*\frac{\partial \mathrm{E}_z}{\partial y} \\ \mathrm{E}_{\circlearrowleft}^*\frac{\partial \mathrm{E}_{\circlearrowleft}}{\partial z}+\mathrm{E}_{\circlearrowright}^*\frac{\partial \mathrm{E}_{\circlearrowright}}{\partial z}+\mathrm{E}_z^*\frac{\partial \mathrm{E}_z}{\partial z} \end{pmatrix}. \quad (15)$$

Nevertheless, the mode confinement in a slab much thinner than the wavelength, as is the case here, implies that the fields remain mostly TE by continuity [1]. It implies not only that $\vec{P}_z$ is null in the plane of symmetry and negligible everywhere else, but also that the out-of-plane (in-plane) contribution of the electric (magnetic) field part is null. It allows for $\vec{P}$ to be represented there without losing clarity, as in Figs. 8(a) and 8(b) for the TE_1^+ and TE_1^- modes, respectively, the relevant energy densities have been superimposed. It can be noted that if the energy densities of the LCP and RCP components do not significantly overlap, they are also linked by the glide-plane symmetry as well as their associated linear momentum densities,

$$\epsilon|\vec{\mathrm{E}}_{\circlearrowleft}|^2(x,y,0) = \epsilon|\vec{\mathrm{E}}_{\circlearrowright}|^2(x+a/2,-y,0),$$
$$\begin{pmatrix} \mathrm{E}_{\circlearrowleft}^*\frac{\partial \mathrm{E}_{\circlearrowleft}}{\partial x} \\ \mathrm{E}_{\circlearrowleft}^*\frac{\partial \mathrm{E}_{\circlearrowleft}}{\partial y} \end{pmatrix}(x,y,0) = \begin{pmatrix} -\mathrm{E}_{\circlearrowleft}^*\frac{\partial \mathrm{E}_{\circlearrowleft}}{\partial x} \\ \mathrm{E}_{\circlearrowleft}^*\frac{\partial \mathrm{E}_{\circlearrowleft}}{\partial y} \end{pmatrix}(x+a/2,-y,0), \quad (16)$$

which establish the circular polarization as an appropriate basis to characterize the electric fields of these PCW modes with enhanced chirality. Similar conditions also apply to the

magnetic field part, such that

$$\mu_0|\vec{H}_z|^2(x,y,0) = \mu_0|\vec{H}_z|^2(x+a/2,y,0),$$
$$\begin{pmatrix} H_z^* \frac{\partial H_z}{\partial x} \\ H_z^* \frac{\partial H_z}{\partial y} \end{pmatrix}(x,y,0) = \begin{pmatrix} -H_z^* \frac{\partial H_z}{\partial x} \\ H_z^* \frac{\partial H_z}{\partial y} \end{pmatrix}(x+a/2,y,0). \quad (17)$$

Over and above the fact that Eq. (16) and Eq. (17) imply that the linear momentum densities do not have a net momentum along the propagation direction, it is clear that the longitudinal component of each contribution cancels at $x = a/4$ and $3a/4$. This means that the electromagnetic field flows are normal to the direction of propagation at both the C points and the vortex center locations. As regards the global momentum of the fields, two distinct manners of satisfying the ZGV and the resulting zero total energy flow are observable in the linear momentum densities of the bonding modes. The linear momentum density of the TE_1^+ mode does not propagate due to clear drifts of the fields in the y direction. On the contrary, for the TE_1^- mode, the longitudinal component of the linear momentum density is dominant and the zero overall field displacement is achieved by opposite local currents that emerge from $x = a/4$ and merge to $x = 3a/4$ in each unit cell.

The OAM density is a vector field that represents the orbital motion of the wave through its intensity and its direction; it is therefore normal to the orbital plane of the fields. In order to determine the orbital characteristic of the mode at the local level, the linear momentum density is needed in conjunction with the appropriate centroid of the wave, where the structured field can be considered balanced with respect to the rotation. Nevertheless, due to the periodicity and the lack of mirror symmetry, defining here the origin $\vec{r}_0 = (x, y_0, z_0)$ to calculate the OAM density, and so the frame of reference, is nontrivial, in contrast with waves propagating in continuous media that have a front wave with a constant intensity. As the modes are associated with a global wave vector pointing along $\vec{x}$, it is appropriate to define the OAM density in the yz plane along the x axis. The suitable position to calculate this torque is the energy barycenter, whose y coordinate is defined by

$$y_0(x) = \frac{\int_{-\infty}^{\infty} y(\mu_0|\vec{H}(x,y,z)|^2 + \epsilon|\vec{E}(x,y,z)|^2)dzdy}{\int_{-\infty}^{\infty}(\mu_0|\vec{H}(x,y,z)|^2 + \epsilon|\vec{E}(x,y,z)|^2)dzdy}. \quad (18)$$

Finally, the symmetry along the slab thickness involves that the z coordinate of the energy barycenter is simply $z_0 = 0$, so the OAM density can be rewritten as

$$\vec{L}(x,y,z) = \begin{pmatrix} 0 \\ y - y_0 \\ z \end{pmatrix} \times \vec{P}(x,y,z). \quad (19)$$

To compare the behavior of the OAM density with respect to the spin of light, the former is plotted in the xz plane at y positions containing the C points in Figs. 9(a) and 9(b) for the TE_1^+ and TE_1^- modes, respectively, and are superimposed onto the Stokes parameter S_3. If the OAM density profiles also present a spiral structure in the yz plane, as previously seen for the SAM density, its sense of circulation changes along the propagation because the transverse component of the OAM density is even with respect to the twofold screw axis symmetry. In addition, the longitudinal component is odd

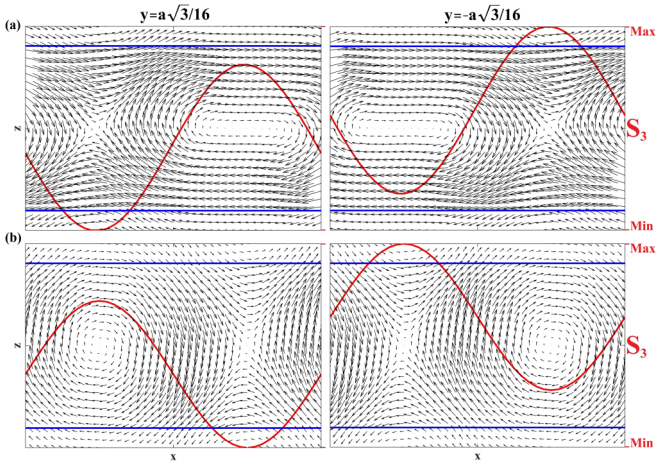

FIG. 9. OAM density of the (a) TE_1^+ and (b) TE_1^- modes in the xz plane represented by black arrows and superimposed on the Stokes parameter $S_3(x, y, 0)$ plotted in red for $y = \pm a\sqrt{3}/16$. The structure is outlined by blue lines.

with respect to the same symmetry:

$$\begin{pmatrix} L_x \\ L_y \\ L_z \end{pmatrix}(x,y,z) = \begin{pmatrix} -L_x \\ L_y \\ L_z \end{pmatrix}(x+a/2,-y,-z). \quad (20)$$

As Eq. (19) implies, the orbital motion of the modes is derived from the orientation of the linear momentum density, and the first consequence of $\vec{P}$ pointing in the xy plane is that the OAM density is exclusively pointing in the z direction in the plane of symmetry. If it once again confirms the photonic wheels character of the AM in the studied structure, another effect arises from the fact that $P_x(a/4, y, z) = P_x(3a/4, y, z) = 0$. It constrains the transverse components of the OAM density to cancel at these locations. In addition to that, other symmetry relations emphasize how the OAM density allows the mode to exhibit local fluxes with opposite orbital motion, while maintaining a zero net OAM in the unit cell, namely, the mirror reflection symmetries σ_x at $x = a/4, 3a/4$ and σ_z at $z = 0$. As shown in Fig. 9, these particular symmetries leads to inverse the longitudinal and the transverse component of the OAM density, respectively, as

$$L_{yz}(a/4+\delta x, y, -z) = -L_{yz}(a/4-\delta x, y, z),$$
$$L_{yz}(3a/4+\delta x, y, -z) = -L_{yz}(3a/4-\delta x, y, z),$$
$$L_x(x,y,z) = -L_x(x,y,-z). \quad (21)$$

where δ_x is a displacement along $\vec{x}$. Moreover, the landscapes of this field bring into view another aspect of the spin-orbit coupling in the studied PCW, specifically that the opposite OAM circulating fluxes are both merging and emerging from the C points. Despite the close proximity of the C points with opposite handedness in the y direction, the structure of the OAM density abruptly changes to confine spiral flows accordingly. Altogether, it leads to the inversion of the orbital motion exactly at the C-point locations. It is also in agreement with the modified Landau-Lifshitz equation developed in Sec. III, as right- and left-handed orbits gather and scatter exactly where the electric field is fully circularly polarized,

indicating the influence of opposite orbitals on the degree of polarization.

V. CONCLUSION

In summary, it has been shown that breaking the PCW parity can lead to the formation of hybrid modes supporting both enhanced transverse SAM and OAM at anomalous ZGV points. Clear interplays between these two degrees of freedom are noted throughout the paper. Along the major energy streamlines, the motion of polarization on the Poincaré sphere is analogous to helical spin waves and can be described by a modified Landau-Lifshitz equation where the optical vortices play the role of an effective polarization vector. Moreover, the AM densities have been investigated all across the PCW structure in the particular context of the very slow-light regime and reveal a peculiar behavior between the spin and the orbital parts of the AM. The SAM density has been found to be generated by the optical vortices bonding them like an antiferromagnetic material, while the OAM density forms spiral flows that cancel exactly at C points.

Moreover, the detailed study of the AM flows in three dimensions allows one to understand how the spin-orbit coupling can be engineered in subwavelength-based devices like PhCs by means of structural modifications with possible applications such as single nanoparticle sensors with the potential to identify their chirality [25], optical tweezers [61,62], and unidirectional emission of embedded quantum emitters [27,28]. In addition, this coupling between spin and orbital parts of the AM also opens the perspective for controlling one degree of freedom with the other and inducing spin-to-orbital conversion of light and, vice versa [34,63,64], engineering directional routing of light on-chip as well as the spin-Hall effect of light in cleverly tailored nanophotonic components [31]. Moreover, the break of other symmetries can lead to the emergence of a net AM that can be transmitted through the PCW, for example, a waveguide at the interface between two PhCs with different topologies [55]. There is also the potential to engineer the rotation of the OAM, i.e., from longitudinal to transverse or vice versa, by adiabatically interfacing such a PCW holding photonic wheels with a trench waveguide supporting longitudinal OAM [65] modes. Last but not least, other numerous applications can take advantage of the slow-light regime such as nonlinear photonics [6,7] with the benefit of combining it with spin or orbital selection rules.

The data from the paper can be obtained from the University of Southampton ePrint research repository [66].

ACKNOWLEDGMENTS

M.S. and S.S gratefully acknowledge Prof. H. Rutt and D. Burt for fruitful discussions. This work was funded by Engineering and Physical Sciences Research Council (EPSRC) Grants (EP/M009416/1, EP/M008975/1), an EU FP7 People: Marie-Curie Actions (PEOPLE) Grant (PCIG13-GA2013-618116), and the University of Southampton Zepler Institute Research Collaboration Stimulus Fund.

[1] J. D. Joannopoulos, S. G. Johnson, J. N. Winn, and R. D. Meade, *Photonic Crystals: Molding the Flow of Light* (Princeton University Press, Princeton, NJ, 2011).

[2] S. G. Johnson, S. Fan, P. R. Villeneuve, J. D. Joannopoulos, and L. A. Kolodziejski, Guided modes in photonic crystal slabs, Phys. Rev. B **60**, 5751 (1999).

[3] E. Yablonovitch, Inhibited Spontaneous Emission in Solid-State Physics and Electronics, Phys. Rev. Lett. **58**, 2059 (1987).

[4] A. Blanco, E. Chomski, S. Grabtchak, M. Ibisate, S. John, S. W. Leonard, C. Lopez, F. Meseguer, H. Miguez, J. P. Mondia *et al.*, Large-scale synthesis of a silicon photonic crystal with a complete three-dimensional bandgap near 1.5 micrometres, Nature **405**, 437 (2000).

[5] S. Noda, K. Tomoda, N. Yamamoto, and A. Chutinan, Full three-dimensional photonic bandgap crystals at near-infrared wavelengths, Science **289**, 604 (2000).

[6] T. Baba, Slow light in photonic crystals, Nat. Photon. **2**, 465 (2008).

[7] T. F. Krauss, Why do we need slow light? Nat. Photon. **2**, 448 (2008).

[8] Y. A. Vlasov, M. O'boyle, H. F. Hamann, and S. J. McNab, Active control of slow light on a chip with photonic crystal waveguides, Nature **438**, 65 (2005).

[9] M. Notomi, K. Yamada, A. Shinya, J. Takahashi, C. Takahashi, and I. Yokohama, Extremely Large Group-Velocity Dispersion of Line-Defect Waveguides in Photonic Crystal Slabs, Phys. Rev. Lett. **87**, 253902 (2001).

[10] V. S. C. Manga Rao and S. Hughes, Single quantum-dot purcell factor and β factor in a photonic crystal waveguide, Phys. Rev. B **75**, 205437 (2007).

[11] S. Hughes, Enhanced Single-Photon Emission from Quantum Dots in Photonic Crystal Waveguides and Nanocavities, Opt. Lett. **29**, 2659 (2004).

[12] M. Arcari, Immo Söllner, A. Javadi, S. L. Hansen, S. Mahmoodian, J. Liu, H. Thyrrestrup, E. H. Lee, J. D. Song, S. Stobbe *et al.*, Near-Unity Coupling Efficiency of a Quantum Emitter to a Photonic Crystal Waveguide, Phys. Rev. Lett. **113**, 093603 (2014).

[13] G. Milione, H. I. Sztul, D. A. Nolan, and R. R. Alfano, Higher-Order Poincaré Sphere, Stokes Parameters, and the Angular Momentum of Light, Phys. Rev. Lett. **107**, 053601 (2011).

[14] G. Milione, S. Evans, D. A. Nolan, and R. R. Alfano, Higher Order Pancharatnam-Berry Phase and the Angular Momentum of Light, Phys. Rev. Lett. **108**, 190401 (2012).

[15] A. A. Sukhorukov, S. Ha, A. S. Desyatnikov, A. V. Lavrinenko, and Y. S. Kivshar, Slow-light vortices in periodic waveguides, J. Opt. A: Pure Appl. Opt. **11**, 094016 (2009).

[16] M. Burresi, R. J. P. Engelen, A. Opheij, D. V. Oosten, D. Mori, T. Baba, and L. Kuipers, Observation of Polarization Singularities at the Nanoscale, Phys. Rev. Lett. **102**, 033902 (2009).

[17] A. B. Young, A. C. T. Thijssen, D. M. Beggs, P. Androvitsaneas, L. Kuipers, J. G. Rarity, S. Hughes, and R. Oulton, Polarization Engineering in Photonic Crystal Waveguides for Spin-Photon Entanglers, Phys. Rev. Lett. **115**, 153901 (2015).

[18] P. Banzer, M. Neugebauer, A. Aiello, C. Marquardt, N. Lindlein, T. Bauer, and G. Leuchs, The photonic wheel: Demonstration of a state of light with purely transverse angular momentum, J. Euro. Opt. Soc. Rapid Publ. **8**, 13032 (2013).

[19] A. Aiello and P. Banzer, The ubiquitous photonic wheel, J. Opt. **18**, 085605 (2016).

[20] A. Aiello, P. Banzer, M. Neugebauer, and G. Leuchs, From transverse angular momentum to photonic wheels, Nat. Photon. **9**, 789 (2015).

[21] M. Neugebauer, T. Bauer, A. Aiello, and P. Banzer, Measuring the Transverse Spin Density of Light, Phys. Rev. Lett. **114**, 063901 (2015).

[22] K. Y. Bliokh, A. Y. Bekshaev, and F. Nori, Extraordinary momentum and spin in evanescent waves, Nat. Commun. **5**, 3300 (2014).

[23] K. Y. Bliokh and F. Nori, Transverse and longitudinal angular momenta of light, Phys. Rep. **592**, 1 (2015).

[24] F. J. Rodríguez-Fortuño, G. Marino, P. Ginzburg, D. O'Connor, A. Martínez, G. A. Wurtz, and A. V. Zayats, Near-field interference for the unidirectional excitation of electromagnetic guided modes, Science **340**, 328 (2013).

[25] F. J. Rodríguez-Fortuño, I. Barber-Sanz, D. Puerto, A. Griol, and A. Martínez, Resolving light handedness with an on-chip silicon microdisk, ACS Photon. **1**, 762 (2014).

[26] C. Junge, D. O'shea, J. Volz, and A. Rauschenbeutel, Strong Coupling Between Single Atoms and Nontransversal Photons, Phys. Rev. Lett. **110**, 213604 (2013).

[27] I. Söllner, S. Mahmoodian, S. L. Hansen, L. Midolo, A. Javadi, G. Kiršanskė, T. Pregnolato, H. El-Ella, E. H. Lee, J. D. Song *et al.*, Deterministic photon–emitter coupling in chiral photonic circuits, Nat. Nanotech. **10**, 775 (2015).

[28] S. Barik, A. Karasahin, C. Flower, T. Cai, H. Miyake, W. DeGottardi, M. Hafezi, and E. Waks, A topological quantum optics interface, Science **359**, 666 (2018).

[29] K. Y. Bliokh, A. Y. Bekshaev, and F. Nori, Optical momentum and angular momentum in complex media: From the Abraham–Minkowski debate to unusual properties of surface plasmon-polaritons, New J. Phys. **19**, 123014 (2017).

[30] M. F. Picardi, K. Y. Bliokh, F. J. Rodríguez-Fortuño, F. Alpeggiani, and F. Nori, Angular momenta, helicity, and other properties of dielectric-fiber and metallic-wire modes, Optica **5**, 1016 (2018).

[31] M. Onoda, S. Murakami, and N. Nagaosa, Hall Effect of Light, Phys. Rev. Lett. **93**, 083901 (2004).

[32] T. Ma and G. Shvets, All-Si Valley-Hall photonic topological insulator, New J. Phys. **18**, 025012 (2016).

[33] X. D. Chen, F. L. Zhao, M. Chen, and J. W. Dong, Valley-contrasting physics in all-dielectric photonic crystals: Orbital angular momentum and topological propagation, Phys. Rev. B **96**, 020202(R) (2017).

[34] J.-L. Liu, W.-M. Ye, and S. Zhang, Pseudospin-induced chirality with staggered optical graphene, Light: Sci. Appl. **5**, e16094 (2016).

[35] S. Barik, H. Miyake, W. DeGottardi, E. Waks, and M. Hafezi, Two-dimensionally confined topological edge states in photonic crystals, New J. Phys. **18**, 113013 (2016).

[36] L.-H. Wu and X. Hu, Scheme for Achieving a Topological Photonic Crystal by Using Dielectric Material, Phys. Rev. Lett. **114**, 223901 (2015).

[37] A. Yu Petrov and M. Eich, Zero Dispersion at Small Group Velocities in Photonic Crystal Waveguides, Appl. Phys. Lett. **85**, 4866 (2004).

[38] M. Sotto, K. Debnath, A. Z. Khokhar, I. Tomita, D. Thomson, and S. Saito, Anomalous zero-group-velocity photonic bonding states with local chirality, JOSA B **35**, 2356 (2018).

[39] A. Mock, L. Lu, and J. O'Brien, Space group theory and Fourier space analysis of two-dimensional photonic crystal waveguides, Phys. Rev. B **81**, 155115 (2010).

[40] M. Sotto, I. Tomita, K. Debnath, and S. Saito, Polarization rotation and mode splitting in photonic crystal line-defect waveguides, Frontiers Phys. **6**, 85 (2018).

[41] G. Dresselhaus, Spin-orbit coupling effects in zinc blende structures, Phys. Rev. **100**, 580 (1955).

[42] M. Ibanescu, S. G. Johnson, D. Roundy, C. Luo, Y. Fink, and J. D. Joannopoulos, Anomalous Dispersion Relations by Symmetry Breaking in Axially Uniform Waveguides, Phys. Rev. Lett. **92**, 063903 (2004).

[43] M. Ibanescu, S. G. Johnson, D. Roundy, Y. Fink, and J. D. Joannopoulos, Microcavity confinement based on an anomalous zero group-velocity waveguide mode, Opt. Lett. **30**, 552 (2005).

[44] K. Y. Bliokh, A. Y. Bekshaev, and F. Nori, Optical Momentum, Spin, and Angular Momentum in Dispersive Media, Phys. Rev. Lett. **119**, 073901 (2017).

[45] M. R. Dennis, Fermionic out-of-plane structure of polarization singularities, Opt. Lett. **36**, 3765 (2011).

[46] Z.-C. Ren, L.-J. Kong, S.-M. Li, S.-X. Qian, Y. Li, C. Tu, and H.-T. Wang, Generalized Poincare sphere, Opt. Express **23**, 26586 (2015).

[47] S. Yu, X. Piao, and N. Park, Acceleration toward polarization singularity inspired by relativistic $e \times b$ drift, Sci. Rep. **6**, 37754 (2016).

[48] H. Kuratsuji and S. Kakigi, Maxwell-SchröDinger Equation for Polarized Light and Evolution of the Stokes Parameters, Phys. Rev. Lett. **80**, 1888 (1998).

[49] S. Yu, X. Piao, and N. Park, Designing non-Hermitian dynamics for conservative state evolution on the bloch sphere, Phys. Rev. A **97**, 033805 (2018).

[50] F. D. M. Haldane, Nonlinear Field Theory of Large-Spin Heisenberg Antiferromagnets: Semiclassically Quantized Solitons of the One-Dimensional Easy-Axis Néel State, Phys. Rev. Lett. **50**, 1153 (1983).

[51] Y. B. Bazaliy, B. A. Jones, and S.-C. Zhang, Modification of the Landau-Lifshitz equation in the presence of a spin-polarized current in colossal-and giant-magnetoresistive materials, Phys. Rev. B **57**, R3213 (1998).

[52] I. Affleck, Quantum spin chains and the haldane gap, J. Phys.: Condens. Matter **1**, 3047 (1989).

[53] D. O'connor, P. Ginzburg, F. J. Rodríguez-Fortuño, G. A. Wurtz, and A. V. Zayats, Spin–orbit coupling in surface plasmon scattering by nanostructures, Nat. Commun. **5**, 5327 (2014).

[54] K. Y. Bliokh, F. J. Rodríguez-Fortuño, F. Nori, and A. V. Zayats, Spin–orbit interactions of light, Nat. Photon. **9**, 796 (2015).

[55] W.-M. Deng, X.-D. Chen, F.-L. Zhao, and J.-W. Dong, Transverse angular momentum in topological photonic crystals, J. Opt. **20**, 014006 (2017).

[56] K. Busch and S. John, Liquid-Crystal Photonic-Band-Gap Materials: The Tunable Electromagnetic Vacuum, Phys. Rev. Lett. **83**, 967 (1999).

[57] S. G. Johnson and J. D. Joannopoulos, Block-iterative frequency-domain methods for maxwell's equations in a planewave basis, Opt. Express **8**, 173 (2001).

[58] X. Piao, S. Yu, and N. Park, Design of Transverse Spinning of Light with Globally Unique Handedness, Phys. Rev. Lett. **120**, 203901 (2018).

[59] R. J. Glauber, Time-dependent statistics of the ising model, J. Math. Phys. **4**, 294 (1963).

[60] K. Y. Bliokh, A. Y. Bekshaev, and F. Nori, Dual electromagnetism: Helicity, spin, momentum and angular momentum, New J. Phys. **15**, 033026 (2013).

[61] V. Garcés-Chávez, D. McGloin, M. J. Padgett, W. Dultz, H. Schmitzer, and K. Dholakia, Observation of the Transfer of the Local Angular Momentum Density of a Multiringed Light Beam to an Optically Trapped Particle, Phys. Rev. Lett. **91**, 093602 (2003).

[62] A. T. O'neil, I. MacVicar, L. Allen, and M. J. Padgett, Intrinsic and Extrinsic Nature of the Orbital Angular Momentum of a Light Beam, Phys. Rev. Lett. **88**, 053601 (2002).

[63] K. Y. Bliokh, E. A. Ostrovskaya, M. A. Alonso, O. G. Rodríguez-Herrera, D. Lara, and C. Dainty, Spin-to-orbital angular momentum conversion in focusing, scattering, and imaging systems, Opt. Express **19**, 26132 (2011).

[64] K. Y. Bliokh, M. A. Alonso, E. A. Ostrovskaya, and A. Aiello, Angular momenta and spin-orbit interaction of nonparaxial light in free space, Phys. Rev. A **82**, 063825 (2010).

[65] S. Zheng and J. Wang, On-chip orbital angular momentum modes generator and (de) multiplexer based on trench silicon waveguides, Opt. Express **25**, 18492 (2017).

[66] M. Sotto, H. Sala , K. Debnath, I. Tomita, and S. Saito, Dataset for "Spin-orbit coupling of light in photonic crystal waveguides", University of Southampton, https://doi.org/10.5258/SOTON/D0760 (2018).